COMMUNICATION

Additive Manufacturing of a 3D Terahertz Gradient-Refractive Index Lens

Fan Zhou, Wei Cao, Biqin Dong, Timothy Reissman, Weili Zhang,* and Cheng Sun*

Transformation optics (TO) provides a generalized method to design gradient-refractive index (GRIN) optical elements. These GRIN elements consist of spatially varying constitutive properties which exploit the form invariances of Maxwell's equations.[1,2] As a result, controlling the propagating trajectory of the light is formulated as a mathematic problem of space transformation, which maps an original space to a transformed one with coordinate-dependent anisotropic optical properties. Such transformation offers unprecedented capability to design and realize complex optical functionalities that are not possible using conventional design methodologies. On the other hand, using hierarchical assemblies of "artificial atoms", metamaterials are used to create extraordinary optical properties not available in nature. The rapid advancements in the field of metamaterials have led to the flourishing work of many novel photonic devices and phenomena such as negative refractive index,[3–5] artificial magnetism,[6,7] super resolution imaging,[8,9] and invisibility cloaks.[10–12] In particular, metamaterials offer the freedom to control the variation of the effective optical properties, which is uniquely suited to construct the spatially varying optical properties required by GRIN elements. Additionally, the quasi-conformal transformation technique[13–16] can further alleviate the requirements of anisotropic optical properties of metamaterials. Thus, GRIN optical elements can be created using nearly-isotropic dielectrics, which facilitate broader operational frequency bands and less propagation loss.[17] To create GRIN devices, computerized numerical control (CNC) machining were first employed to fabricate a series of customized printed circuit boards (PCBs) or dielectric plates as the metamaterial building blocks.[4,10,18] Their macroscopic feature sizes made them possible to be manually assembled into a large-scale GRIN optical components. Nanofabrication techniques, such as focused ion beam milling and electron beam lithography, were later used to demonstrate creation of various GRIN optical elements including a diffraction grating,[19] carpet cloaks,[20,21] GRIN lenses,[22–24] and metasurfaces,[25,26] but mostly are 2D in nature. Fabricating 3D GRIN invisibility

cloaking devices was then reported by Wegener's group using directly laser writing process employing two-photon polymerization and later stimulated emission depletion principle in achieving deep sub-wavelength resolution.[11,27] However, the issues with these fabrication techniques have intrinsically been associated with nonscalability as the sophisticate 3D structures are fabricated in a point-by-point serial fashion. Therefore, efficient 3D scalable fabrication techniques are needed to implement intricate GRIN optical elements for increased scalability and extension of working frequencies to broader ranges in the electromagnetic spectrum. Commercial 3D printers have been used widely in manufacturing industries to make parts with millimeter features. However, they still lack the capability to create GRIN metamaterials, with both the optically large overall size and strictly accurate sub-wavelength structures.

In this paper, we present a powerful additive manufacturing technique—projection microstereolithography (PµSL) for creation of 3D GRIN metamaterials that can operate at the terahertz (THz) frequency band. The THz band is one of the most important but underdeveloped spectrum regions. Its spectra can carry unique absorption fingerprints characterizing molecular vibrational modes and provide information that is not available in the rest of the electromagnetic spectrum.[28] The PµSL technique enables a scalable and rapid way to produce feature sizes down to tens of microns that meets the demand of THz metamaterials. To illustrate these claims, we demonstrate a THz GRIN lens that possesses a continuous index variation from 1.1 to 1.64 and delivers a resolution close to the diffraction limit from 0.4 to 0.6 THz, which are sufficient for broadband THz TO devices. The index variation is fully controlled by accurately constructing the polarization-independent woodpile-like structure in a layer-by-layer fashion under the effective media approximation. The experimental results show the lens effectively improves the imaging capability compared to a homogeneous spherical lens with nonignorable aberration. Our work represents the convergence of TO designed metamaterials and additive manufacturing. The integration sets the stage for realization of a variety of intriguing THz applications with unprecedented functionalities.

In THz optics, the design and manufacture of optical elements, such as lenses, plays a critical role in controlling THz waves. Many plastics make suitable THz lenses, but they are difficult to fabricate with the tight tolerances necessary for high-quality imaging. Semiconductors and other dielectrics, such as silicon, are also difficult to manufacture and generally suffer from high Fresnel losses due to their high dielectric permittivity. Usually such dielectrics have fixed permittivity and the entire operation of the optics relies on careful crafting of its shape. The undesired imaging aberration is particularly recognizable

Dr. F. Zhou, Dr. B. Dong, Dr. T. Reissman, Prof. C. Sun
Mechanical Engineering Department
Northwestern University
Evanston, IL 60208, USA
E-mail: c-sun@northwestern.edu
Dr. W. Cao, Prof. W. Zhang
School of Electrical and Computer Engineering
Oklahoma State University
Stillwater, OK 74078, USA
E-mail: weili.zhang@okstate.edu

www.MaterialsViews.com

ADVANCED
OPTICAL
MATERIALS
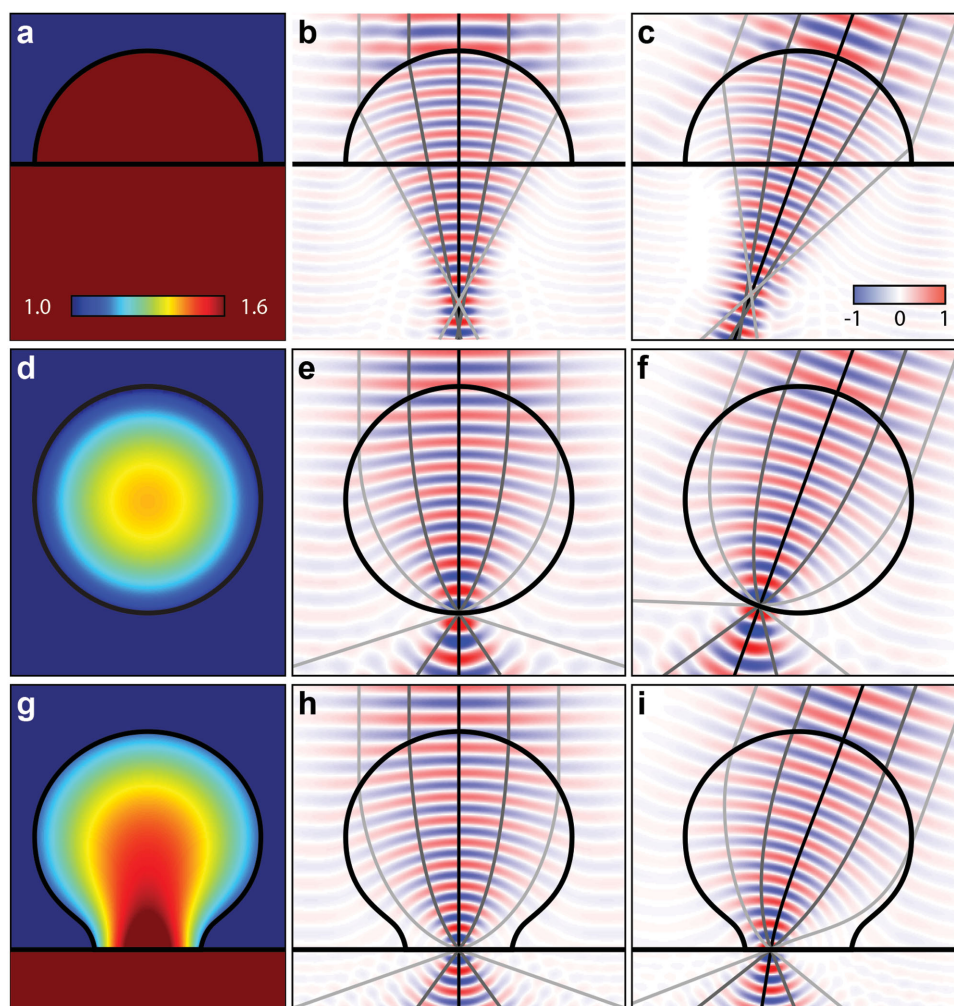www.advopticalmat.de

COMMUNICATION

Figure 1. Comparison of three designs of lenses. The left column shows the refractive index profile; the middle and right columns show the amplitude distribution when normal incidence and oblique incidence occur, respectively. a–c) The homogeneous spherical lens. Lights refracted from different angles focus on different points due to lens' intrinsic aberration. d–f) The spherical Luneburg lens. The parallel rays coming through the lens from any direction can be focused to a point on the opposite side of the sphere without any aberration. Note that the focal plane is spherical and not compatible with flat plane imaging applications. g–i) The transformed Luneburg lens. It not only preserves the unique aberration-free characteristic of the original Luneburg lens design, but also possesses a flat imaging plane.

for the spherical lens shown in **Figure 1**a–c, in which the imaging resolution of a single refractive lens becomes deteriorative due to the classical spherical aberration. Therefore, many modern imaging systems take advantage of stacking several lenses to deliver optimal imaging performance with lower aberrations, however, at the great expense of increased cost and complexity. A feasible solution is the use of GRIN materials,[29–31] which possess a gradient in the refractive index and guide light rays to bend within the material. As a representative example, the spherical Luneburg lens,[32] that has a radially decreasing refractive index, can focus the collimated light to a point on its surface from a wide angle range without any aberrations (Figure 1d–f).

In practice, with the adoption of the TO theory and metamaterials, a lens with a GRIN profile can be produced with an arbitrary shape to accommodate any THz optics. To make the spherical Luneburg lens compatible with traditional planar detectors or source arrays, a quasi-conformal transformation can be applied to reconfigure the spherical focal plane into a flattened one.[15,33] As shown in Figure S1 of the Supporting Information, the transformed region corresponds to the angular range of ±41.4°, which is the theoretical limit of the incident angle that this particular transformed Luneburg lens can handle. It should be noted that the refractive index in the resulting transformed Luneburg lens varies from 0.451 to 1.719. There are small regions with the refractive index exceeding the range that our dielectric metamaterial can achieve. An approximation has been made in the design to replace the region (n < 1) by the region (n = 1.1), while set the upper limit of the refractive index to 1.64. The simulation results clearly suggest the transformed design with approximations has the desirable planar focal plane features, while at the greatest extent preserving the unique aberration-free characteristic of the original Luneburg lens design (Figure 1g–i). When extending the planar design to the third dimension, a trade-off inevitably exists between scalable fabrication of complicated materials and strict
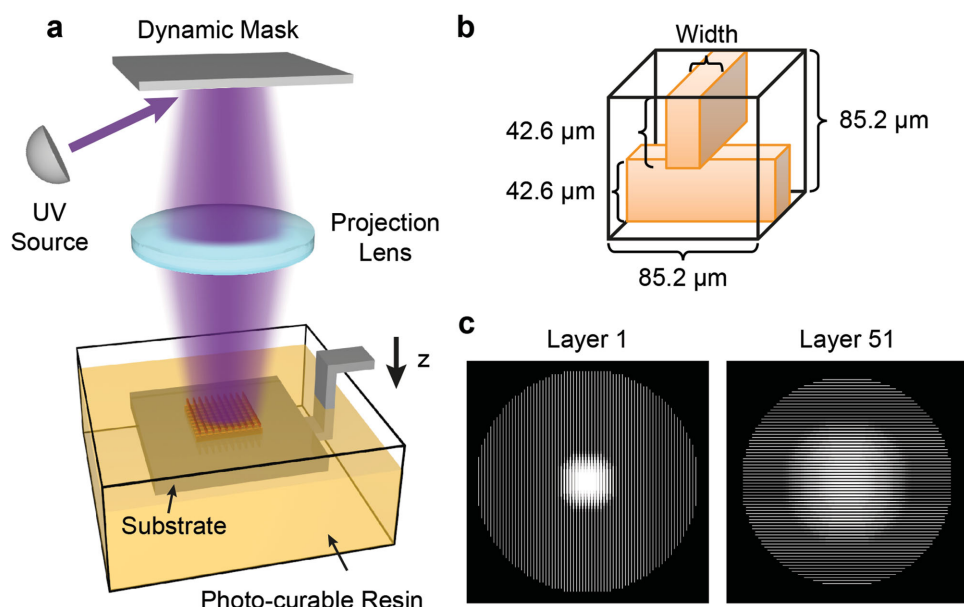
Figure 2. Schematic diagram of projection microstereolithography process for fabricating the GRIN lens. a) 3D CAD design is sliced into serials of 2D patterns and then displayed as a bitmap image on the dynamic mask. The UV light illuminated on the patterned mask is shaped, transferred through a projection lens, and finally directly projects on the top surface of photo-curable polymer resin in high resolution ($7.1 \times 7.1 \ \mu m^2$ per pixel). The sample substrate is mounted on the Z-stage, which can move in the vertical direction with minimum step of 0.5 μm. The liquid resin under the illuminated light (white area in the mask) will be cured into a solid layer. Then the mask is switched to black to prevent further exposure and the structure is lowered by a motorized Z-stage to allow next liquid layer to be cover the top. By repeating these fabrication steps for each layer, highly complicated 3D structures according to the designed geometry can be accomplished from the bottom-up rapidly. b) Each unit cell has a cubic shape with side length of 85.2 μm. It consists of two orthogonal polymer bars and each bar is 42.6 μm thick. By changing the width of the polymer bars, one can precisely control the volume ratio of polymer to air in each unit cell, such that the refractive index can be tuned in the desired manner. c) The grayscale bitmap images are used to tune the width of each polymeric rod in sub-pixel accuracy. Here the bitmap mask for layer 1 (the most bottom layer) and layer 51 are shown.

3D transformation.[34,35] A quasi-3D solution might be achieved by rotating the 2D gradient-index profile about the z-axis, which has been previously employed in the experimental demonstration of a collimation lens at microwave frequencies.[36]

The PμSL process shown in **Figure 2**a is employed to make the 3D transformed GRIN lens. The process involves using a computer-programmable liquid-crystal-on-silicon (LCoS) display chip as the dynamic mask, with a resolution of 1400×1050 and a contrast ratio of 1000:1. By toggling the voltage applied to each individual pixel with the size of $10.65 \times 10.65 \ \mu m^2$, the orientation of liquid crystal molecules can be switched between stable positions, with the light reflecting "on" and "off" directions. The LCoS display offers a fast and highly efficient method of spatially modulating light over a broad range of wavelengths. The computer aided design (CAD) model is sliced into a sequence of 2D bitmap images, which are then loaded to the LCoS display. By illuminating the LCoS display with an ultraviolet (UV) light (405 nm), the patterned light passes through the projection lens (60 mm, f/4, Jenoptik) with a reduction ratio of 1.5:1 and projects onto a photosensitive resin (1,6-hexanediol diacrylate, Sigma-Aldrich, Supporting Information). Using this process, only the desired regions are exposed and cured. Depending on the pixel size on the LCoS display and the projection lens, the system implements approximately $1 \times 0.75 \ cm^2$ in total fabrication area with the x–y resolution of 7.1 μm. Vertical stepping (down to 0.5 μm) generates high-fidelity 3D parts and is accomplished using a z-axis translation stage (Aerotech). In each layer, the illuminated area is solidified

simultaneously under one exposure, while the dark regions remain liquid. A complex, geometrically shaped structure with multiple dimension features from micrometers to millimeters can be fabricated rapidly (over 100 μm min⁻¹) by building all the layers sequentially and stacking them from bottom to top. Depending on The usage of the LCoS display eliminates the need for expensive and time-consuming physical mask fabrication, which are steps normally required for conventional silicon microfabrication processes. All of which makes PμSL an effective and efficient tool for prototyping 3D THz metamaterial devices.

Building upon the unique fabrication capabilities of PμSL, we explored and investigated the 3D GRIN lens using nonresonant metamaterials. Under the effective media approximation,[37] the local refractive index was tuned by subtly varying the polymer volume-filling-ratio of each unit cell, in which the variation in the refractive index was truncated to the range within 1.1 to 1.64 ($\Delta n = 0.54$). In our design, each cubic unit cell (side length: 85.2 μm, Figure 2b) consisted of two orthogonal polymer rods (thickness: 42.6 μm), whose dimensions were one order of magnitude smaller than the vacuum wavelength of the THz wave (≈500 μm). Thus, the metamaterial unit cell created nearly isotropic optical properties near the center of the first Brillouin zone. The designed gradient-index profile was converted into the geometry of the polymer rod with varying width and density in the form of a bitmap image. Grayscale level (G) ranging from 0 (fully black/no exposure) to 255 (fully white/strongest exposure) was used to replace the binary image and

render a modest exposure. Any values between them provided an intermediate value of exposure and effectively changed the degree of polymerization, making the dimensions of polymer rod change smoothly (Figure 2c). Thus, designed line pattern consists of N fully white pixels ($N \geq 1$) across its width with 2 additional gray pixels at both ends. Using a simplified linear approximation, the width of the fabricated polymer rod can be estimated as $W = (2G/255 + N)d$,[38] where d corresponds to the pixel width (7.1 µm) of the PµSL system. Thus, tuning the grayscale of the dynamic mask further allow us to fine the width of polymer rod at sub-pixel level accuracy. However, it is worthwhile to note that photopolymerization is a nonlinear process. Although the linear model being used in this study yields reasonable results, in case the higher fabrication precision is desired, more sophisticate process model will be needed to fully capture the nonlinear process characteristics.[39] The stack of the bitmap images was then programmed into the PµSL system to directly print the 3D THz lens, with the desired refractive index distribution.

Figure 3a illustrates the physical, transformed GRIN lens with complex 3D microscale geometries, which was fabricated out of photopolymer material using the PµSL process and was optically large in all three dimensions. The entire lens has a total height of 4.27 mm and is comprised of 100 layers of neatly arranged polymer rod array, corresponding to over 120 000 defect-free unit cells. The fabrication took approximately 40 min, as each layer is photopolymerized using a single optical exposure. Since the intensity of the individual pixels was further tuned at grayscale levels, the desired refractive index distribution had smooth spatial transitions, which minimized the scattering of the THz wave. As shown in Figure 3b, the woodpile structures were fabricated with high precision. The cross-sectional view shown in Figure 3c illustrates the effective transformation of the spatial variation of polymer volume-filling-ratio to the refractive index distribution. The imaging performance of the THz lens was characterized by employing a fiber-based, angular-resolved terahertz time-domain spectroscopy (THz-TDS) technique,[40,41] as shown in Figure 3d. Here, a metallic mask was used as the imaging sample and placed against the flattened imaging region to selectively allow the transmission of the THz wave. The metallic mask was fabricated in a 50 µm thick stainless steel film using laser micromachining process
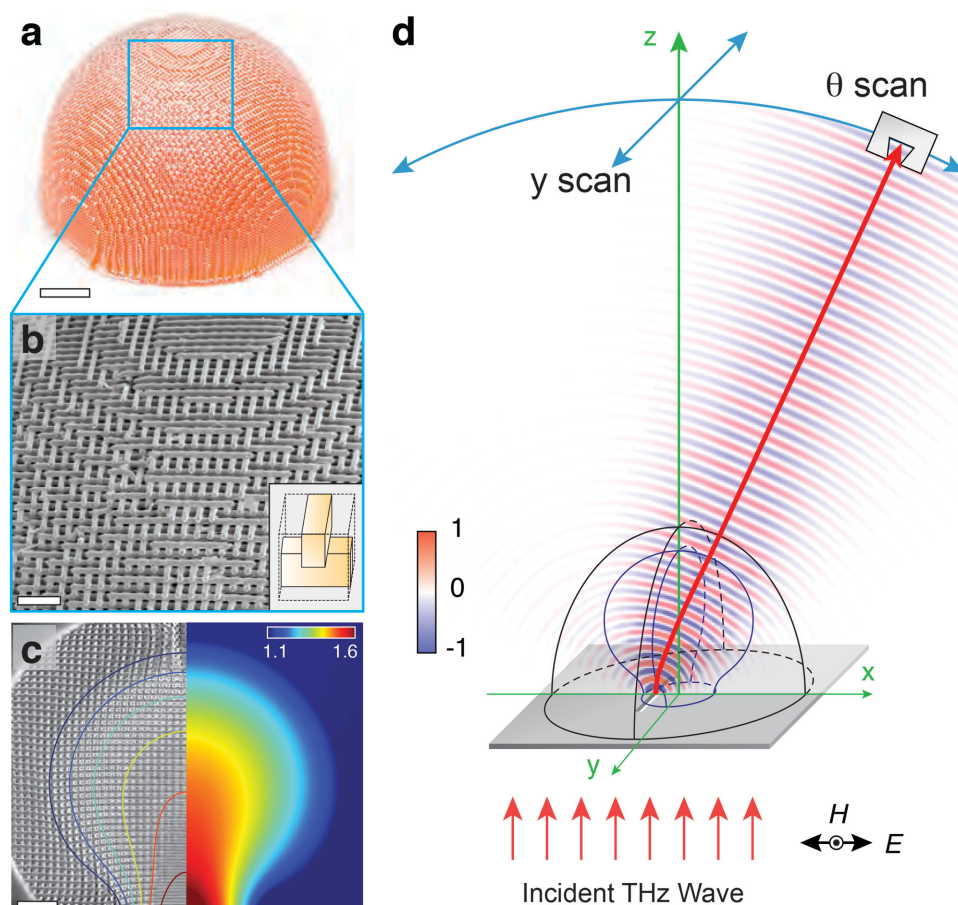

Figure 3. 3D THz GRIN lens. a) The fabricated lens is made of 100 layers of polymeric woodpile-like structure. Bar: 2 mm. b) Scanning electron images of the lens composed of clear woodpile structures with high precision. The subset shows the unit cell structure that is illustrated in Figure 2b. Bar: 300 µm. c) Cross-sectional view shows the varied dense of "woodpiles", which well represents the gradually changed index distribution shown in the right half of the figure. Bar: 500 µm. d) Schematic of imaging single-slit object with the proposed GRIN lens. At far field, detector moves along the circle in θ–z plane and along straight line in y–z plane to scan THz signals.

ADVANCED
OPTICAL
MATERIALS
www.advopticalmat.de

Materials
Views
www.MaterialsViews.com

with a resolution of 10 µm. To condition the incident wave, a photoconductive switch-based THz-TDS system was optically gated by 30 fs, 800 nm optical pulses generated from a self-mode-locked Ti:sapphire laser. The THz radiation, emitted from a GaAs transmitter, was spatially gathered by a hyper-hemispherical silicon lens and then collimated into a parallel beam before entering the test sample at normal incidence. The transmitted THz far-field signal was detected by a mobile silicon-on-sapphire (SOS) receiver, which was optically triggered by fiber-coupled femtosecond pulses. The detector was placed 20 mm away from the output interface of the imaging sample and scanned in 2D space to measure the spatial distribution of the transmitted THz wave-front at the far-field. The frequency-dependent THz amplitudes at each spatial position were then retrieved via a Fourier transform of the measured time-domain signals.

The imaging characteristic of the fabricated GRIN lens was first evaluated by placing a metallic mask containing a 200 µm wide single slit at the flattened focal plane. While progressively shifting the slit away from the center, the angular distribution of the refracting collimated THz beam was then characterized by scanning the detector in the θ-z plane (Figure 3d). **Figure 4** shows the comparison of experimental results with simulations at the representative frequency of 0.5 THz for five separate cases. The horizontal and vertical axes represent angular positions and frequencies, respectively, while the color represents the amplitude of the THz wave being normalized to the peak value of the first measurement (Figure 4a). When the slit was placed at the center of the focal plane, the measurement result illustrated that the wave propagates along the z-axis with a broadband frequency ranging from 0.4 to 0.6 THz. This is in good agreement with the simulation that indicates a nearly planar wave-front at the far field (Figure S2, Supporting Information). The refraction angle increased progressively when the slit translated away from the center. When the slit moved as far as 500 µm away from the center (Figure 4f), the refraction angle reached approximately 21.2° due to the limitation of the flattened region (Figure S2, Supporting Information). The full-width half-maximum (FWHM) of the measured peaks have constant values of 8.6° ± 1.5° at all refraction angles. The simulated peak positions of the refracted beam at the center frequency of 0.5 THz were superimposed onto the experimental results as white solid lines (Figure 4). The experimentally measured refraction angles are in good agreement with the simulation results (Figure S3, Supporting Information) and show a nearly linear behavior with respect to the off-center location of the slit. These demonstrate that the fabricated GRIN lens features the consistent imaging characteristic over the field of view, which is determined by the flattened focal plane.

Next, we evaluated the imaging resolution of the GRIN lens using a double-slit object with a width of 200 µm and an edge-to-edge distance of 300 µm. Both simulation and experimental results, as shown in **Figure 5**a,b, respectively, indicate the double-slit feature to be well resolved over the same THz spectra of 0.4 to 0.6 THz. In Figure 5b, we include white circles to represent the peak position obtained from numerical simulations, which indicate good agreement between theory and experiment. One should note that at 0.4 THz, the resolved feature size was very close to the diffraction limit resolution
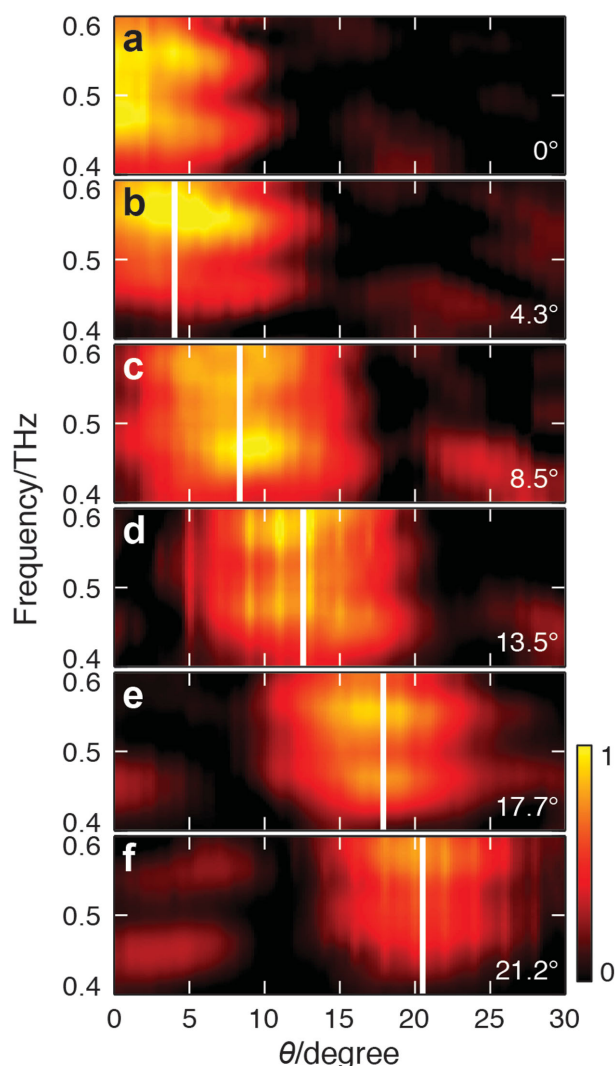

Figure 4. Steering the THz wave using the GRIN lens. a–f) Experimental spectra maps are measured when a line source positioned from the center to 100, 200, 300, 400, and 500 µm off the center, respectively. White lines indicate simulated peak positions of the refracted THz wave at 0.5 THz and their bending degrees are marked on the right for clarity. Note that the transmitted THz wave is bended from 0° to 21.2° when the line source moves from the center to 500 µm off the center.

of 279 µm, which was estimated using the highest index of the transformed lens. This results in an additional center peak below 0.45 THz when the feature size reaches to the diffraction limit. To contrast these results, in the control case of a spherical lens made of homogenous dielectric material (n = 1.64), the simulation results shown in Figure 5c indicate that the double-slit feature was no longer resolvable at frequency below 0.5 THz due to lens' intrinsic spherical aberration. The additional center peak found at the frequency above 0.52 THz is likely due to the multiple scattering by the woodpile structure at higher frequency. Such issue can potentially be solved by scaling down the dimension of the unit cell. To better illustrate the difference, the calculated and measured THz amplitudes at 0.5 THz for the aforementioned three cases are shown in Figure 5d. Plots of experimental measurement (red circles)

www.MaterialsViews.com

ADVANCED
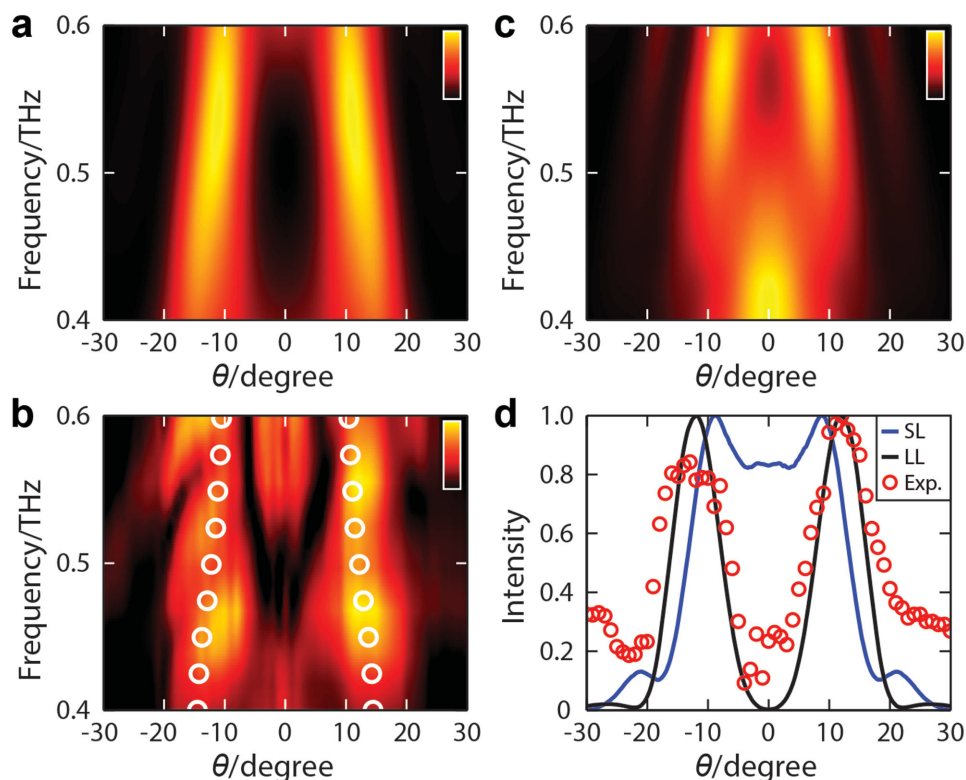OPTICAL
MATERIALS
www.advopticalmat.de

COMMUNICATION

Figure 5. A 300 μm edge-to-edge spaced double-slit object is imaged by the GRIN lens. a) The simulation spectra map shows the double-slit feature can be clearly resolved over a broadband from 0.4 to 0.6 THz by using the GRIN lens. b) The experimental result exhibits two obvious spatial maxima, which match very well with the simulated values (white circles) extracted from (a). c) The simulation result shows a uniform spherical lens (n = 1.64) can only resolve the double-slit feature above 0.5 THz due to the existence of geometrical aberration. d) Intensity as function of detector position for above three cases at 0.5 THz. Experimental and simulation results of imaging with GRIN lens have similar intensity distribution, which are distinct from the simulation result of imaging with uniform spherical lens, showing excellent imaging performance.

and simulation (dark line) with the transformed GRIN lens resemble each other very closely, clearly illustrating two separated peaks, which demonstrates the double-slit to be resolved. In contrast, the curve of imaging with the uniform spherical lens (blue line) only exhibits two minor peaks that are difficult to resolve. These results suggest that the GRIN lens significantly improves the resolution in contrast to the uniform spherical lens.

In summary, we have experimentally demonstrated an effective THz GRIN lens, which was designed by transforming a spherical Luneburg lens using TO theory. Building upon the polarization independent metamaterial unit cells, this singlet GRIN lens was fabricated using the PµSL process. It was characterized using THz-TDS system and delivered an imaging resolution very close to the diffraction limit over a frequency range from 0.4 to 0.6 THz. This performance was shown to yield better imaging capabilities than the uniform spherical lens, specifically with respect to aberration. Due to the synergistic combination of theory, characterization, and particularly scalable 3D fabrication, we envision our work to enable realization of new fundamental advances in compact THz optical systems with superior capability to control the flow of THz waves. Of perhaps the highest importance, the integration of our PµSL method for additive manufacturing opens a new route to achieve these 3D THz metamaterials.

Supporting Information

Supporting Information is available from the Wiley Online Library or from the author.

Acknowledgements

[1] J. B. Pendry, D. Schurig, D. R. Smith, *Science* **2006**, *312*, 1780.
[2] U. Leonhardt, *Science* **2006**, *312*, 1777.
[3] C. G. Parazzoli, R. B. Greegor, K. Li, B. E. C. Koltenbah, M. Tanielian, *Phys. Rev. Lett.* **2003**, *90*, 107401.
[4] R. A. Shelby, D. R. Smith, S. Schultz, *Science* **2001**, *292*, 77.
[5] J. B. Pendry, D. R. Smith, *Phys. Today* **2004**, *57*, 37.
[6] T. J. Yen, W. J. Padilla, N. Fang, D. C. Vier, D. R. Smith, J. B. Pendry, D. N. Basov, X. Zhang, *Science* **2004**, *303*, 1494.

ADVANCED
OPTICAL
MATERIALS
www.advopticalmat.de

Materials
Views
www.MaterialsViews.com

[7] B. Dong, X. Chen, F. Zhou, C. Wang, F. H. Zhang, C. Sun, **2015**, arXiv: 1508.07683. arXiv.org e-Print archive. http://arxiv.org/abs/1508.07683 (accessed: April 2016).

[8] N. Fang, H. Lee, C. Sun, X. Zhang, *Science* **2005**, *308*, 534.

[9] Z. W. Liu, H. Lee, Y. Xiong, C. Sun, X. Zhang, *Science* **2007**, *315*, 1686.

[10] D. Schurig, J. J. Mock, B. J. Justice, S. A. Cummer, J. B. Pendry, A. F. Starr, D. R. Smith, *Science* **2006**, *314*, 977.

[11] T. Ergin, N. Stenger, P. Brenner, J. B. Pendry, M. Wegener, *Science* **2010**, *328*, 337.

[12] X. Ni, Z. J. Wong, M. Mrejen, Y. Wang, X. Zhang, *Science* **2015**, *349*, 1310.

[13] N. I. Landy, W. J. Padilla, *Opt. Express* **2009**, *17*, 14872.

[14] H. Chen, C. T. Chan, P. Sheng, *Nat. Mater.* **2010**, *9*, 387.

[15] J. P. Turpin, A. T. Massoud, Z. H. Jiang, P. L. Werner, D. H. Werner, *Opt. Express* **2010**, *18*, 244.

[16] L. Xu, H. Chen, *Nat. Photonics* **2015**, *9*, 15.

[17] J. S. Li, J. B. Pendry, *Phys. Rev. Lett.* **2008**, *101*, 203901.

[18] R. Liu, C. Ji, J. J. Mock, J. Y. Chin, T. J. Cui, D. R. Smith, *Science* **2009**, *323*, 366.

[19] Y. J. Tsai, S. Larouche, T. Tyler, G. Lipworth, N. M. Jokerst, D. R. Smith, *Opt. Express* **2011**, *19*, 24411.

[20] J. Valentine, J. S. Li, T. Zentgraf, G. Bartal, X. Zhang, *Nat. Mater.* **2009**, *8*, 568.

[21] M. Gharghi, C. Gladden, T. Zentgraf, Y. Liu, X. Yin, J. Valentine, X. Zhang, *Nano. Lett.* **2011**, *11*, 2825.

[22] T. Zentgraf, J. Valentine, N. Tapia, J. Li, X. Zhang, *Adv. Mater.* **2010**, *22*, 2561.

[23] T. Zentgraf, Y. Liu, M. H. Mikkelsen, J. Valentine, X. Zhang, *Nat. Nanotechnol.* **2011**, *6*, 151.

[24] A. Di Falco, S. C. Kehr, U. Leonhardt, *Opt. Express* **2011**, *19*, 5156.

[25] F. Aieta, P. Genevet, M. A. Kats, N. F. Yu, R. Blanchard, Z. Gahurro, F. Capasso, *Nano Lett.* **2012**, *12*, 4932.

[26] P. R. West, J. L. Stewart, A. V. Kildishev, V. M. Shalaev, V. V. Shkunov, F. Strohkendl, Y. A. Zakharenkov, R. K. Dodds, R. Byren, *Opt. Express* **2014**, *22*, 26212.

[27] J. Fischer, T. Ergin, M. Wegener, *Opt. Lett.* **2011**, *36*, 2059.

[28] F. F. John, S. Brian, H. Feng, G. Dale, B. Robert, O. Filipe, Z. David, *Semicond. Sci. Technol.* **2005**, *20*, S266.

[29] D. T. Moore, *Appl. Opt.* **1980**, *19*, 1035.

[30] W. H. Southwell, *Opt. Lett.* **1983**, *8*, 584.

[31] D. R. Smith, J. J. Mock, A. F. Starr, D. Schurig, *Phys. Rev. E* **2005**, *71*, 036609.

[32] D. Schurig, *New J. Phys.* **2008**, *10*, 115034.

[33] N. Kundtz, D. R. Smith, *Nat. Mater.* **2010**, *9*, 129.

[34] T. Driscoll, G. Lipworth, J. Hunt, N. Landy, N. Kundtz, D. N. Basov, D. R. Smith, *Opt. Express* **2012**, *20*, 13262.

[35] N. I. Landy, N. Kundtz, D. R. Smith, *Phys. Rev. Lett.* **2010**, *105*, 193902.

[36] H. F. Ma, T. J. Cui, *Nat. Commun.* **2010**, *1*, 124.

[37] A. Sihvola, *Electromagnetic Mixing Formulas and Applications*, The Institution of Engineering and Technology, Stevenage, Hertfordshire, UK **1999**.

[38] F. Zhou, Y. Bao, W. Cao, C. Stuart, W. Zhang, C. Sun, *Sci. Rep.* **2011**, *1*, 78.

[39] C. Sun, N. Fang, D.M. Wu, X. Zhang, *Sens. Actuator, A* **2005**, *121*, 113.

[40] D. Grischkowsky, S. Keiding, M. Vanexter, C. Fattinger, *J. Opt. Soc. Am. B* **1990**, *7*, 2006.

[41] M. T. Reiten, S. A. Harmon, R. A. Cheville, *J. Opt. Soc. Am. B* **2003**, *20*, 2215.

COMMUNICATION